Materials Science & Engineering A 908 (2024) 146758

Contents lists available at ScienceDirect

Materials Science & Engineering A

journal homepage: www.elsevier.com/locate/msea

Hardness and microstructural evolution of CoCrFeNi high-entropy alloys during severe plastic deformation

Haihong Jiang [a,*], Qingmei Gong [a,**], Martin Peterlechner [a,b], Lydia Daum [a], Harald Rösner [a], Gerhard Wilde [a,***]

[a] University of Münster, Institute of Materials Physics, 48149, Münster, Germany
[b] Karlsruhe Institute of Technology, Laboratory for Electron Microscopy, 76131, Karlsruhe, Germany

ARTICLE INFO

Keywords:
High-entropy alloy
High-pressure torsion
Deformation mechanism
Microstructural evolution
Ultrafine grained material

ABSTRACT

In this study, the evolution of hardness and microstructure in a CoCrFeNi high-entropy alloy processed by high-pressure torsion was investigated. An initial increase in hardness was attributed to the rapid increase in low-angle grain boundaries (LAGBs), accompanied by a high density of dislocations. With continuous straining, some LAGBs evolved into high-angle grain boundaries and completed the grain boundary strengthening. A remarkable increase in hardness was achieved in the final stage of hardness enhancement, primarily due to the formation of numerous twins within nanograins, which were mainly formed by the emission of Shockley partial dislocations emerging from grain boundaries. Furthermore, a twin trailing the stacking fault was found in the nanograin, and a critical stress for twin nucleation was estimated to be about 2.16 GPa. Defects with low-energy configurations are closely correlated with the thermal stability of nanocrystalline CoCrFeNi alloys. The defects within nanograins yielded an average strain of about 1.1 % and the corresponding strain energy was identified to about 17 J g^{-1}.

1. Introduction

In recent years, high-entropy alloys (HEAs) have been extensively investigated due to their remarkable mechanical properties [1]. The mechanical properties of HEAs strongly depend on their structures, and the most studied structure in HEAs is the face-centered cubic (FCC) phase [2]. Among these HEAs, the equi-atomic CoCrFeNi alloy stands out owing to the highly stable single FCC phase, and thus frequently serves as a base alloy in HEA design for achieving comprehensive properties. As reported in the literature, the matrix alloy of CoCrFeNi exhibits unique properties involving high hardness and good thermal stability [3–5].

Hardness is one of the most regularly emphasized characteristics in evaluating material properties, and grain refinement provides a highly effective means for hardening [6]. When grain sizes are reduced to the nanoscale, such nanostructured materials often offer superior mechanical properties [7]. One of the most powerful approaches for fabricating bulk nanocrystalline materials, without any contamination or porosity, is through severe plastic deformation. In this context, high-pressure torsion (HPT) was thus applied to achieve fully dense material with nanometer-sized grains [8]. In the present study, the evolution of hardness and the corresponding microstructures were characterized to investigate the deformation mechanisms of the HPT-processed CoCrFeNi alloys.

Wang et al. [9] proposed for CoCrFeNi alloys that dislocation-dominated hardening occurred at strains below about 0.4, giving rise to a sharp increase in dislocation density, which was attributed to the readily generation of dislocations in an early-stage of deformation [10]. Gubicza et al. [3] studied the variations of hardness and microstructures of a CoCrFeNi alloy during HPT, and observed a significant increase in the fraction of low-angle grain boundaries (LAGBs) under a shear strain of 4.5. One suggestion is that LAGBs formed at a low strain, and are difficult to be annihilated because of the low stacking fault energy (SFE) of CoCrFeNi alloys [10]. With further straining, a significant hardness increase at a strain of 12 was reported, and grain boundary (GB) mediated mechanisms were proposed to be

* Corresponding author.
** Corresponding author.
*** Corresponding author.
E-mail addresses: hjiang@uni-muenster.de (H. Jiang), qgong@uni-muenster.de (Q. Gong), gwilde@uni-muenster.de (G. Wilde).

https://doi.org/10.1016/j.msea.2024.146758
Received 11 March 2024; Received in revised form 4 May 2024; Accepted 30 May 2024
Available online 31 May 2024

operational in the HPT-processed CoCrFeNi alloys [11]. However, detailed reports elucidating the governing mechanisms of the hardening process of the HPT-processed CoCrFeNi alloys are still lacking. To date, there is a scarcity of reports elucidating the hardening mechanisms throughout the entire hardening process of CoCrFeNi alloys, spanning from small shear strains (below 1) to very large strains (around 300). Despite numerous deformation studies conducted on CoCrFeNi and its derivatives, this study aims to address this knowledge gap.

In addition, the high thermal stability of CoCrFeNi alloys has been extensively reported in recent years. The high hardness value (~ 5.1 GPa) of the HPT-processed CoCrFeNi alloys remained stable up to a temperature of around 750 K [12]. Meanwhile, a high work-hardening rate based on twin formation was achieved through high-temperature annealing at about 1073 K [13]. Surprisingly, sintered CoCrFeNi alloys exhibited exceptional thermal stability, retaining their properties even after annealing at a temperature of 973 K for 600 h [5]. Although the high stability of the microstructure in CoCrFeNi alloys has been widely accepted in the past few years, He et al. [14] found evidence of phase separation in CoCrFeNi after long-term annealing (1023 K for 800 h). However, there is a lack of literature addressing the factors contributing to the remarkable microstructural stability observed in nanocrystalline CoCrFeNi alloys, a topic explored in this study. Furthermore, the critical stress for twin nucleation and the capacity for strain energy storage post-deformation were also examined.

2. Material and methods

2.1. Sample preparation

Cylindrical ingots of $Co_{25}Cr_{25}Fe_{25}Ni_{25}$ (at.%) HEAs were synthesized by arc melting. In the following, the term "CoCrFeNi" will be employed to specify the material. Four pure components with a purity of at least 99.95 wt.% were alloyed, flipped and re-melted five times in a Ti-gettered high purity argon atmosphere to improve homogeneity. The ingots were then cast into a water-cooled copper mold to obtain cylindrical rods with a length of 30 mm and a diameter of 8 mm. Using a wire electrical discharge machine, disks from the cylindrical center with a thickness of 1 mm were obtained by slicing the rods along their length direction and subsequently sealed in quartz tubes under an argon atmosphere and homogenized at 1373 K for 72 h, followed by water quenching. The homogenized samples were further ground using SiC papers to remove any oxide layers. A dimension of 0.8 mm in thickness and 7.5 mm in diameter was finally obtained for processing in HPT.

2.2. Experimental methods

A custom-designed quasi-constrained HPT device equipped with two anvils was utilized, as shown in Appendix A. Both anvils were machined with the same cavity dimensions, having a depth of 0.3 mm and a diameter of 7.5 mm. Specifically, the finial thickness of the HPT-processed sample is approximately 0.6 mm. The samples were compressed under a hydrostatic pressure of 4.2 GPa at room temperature for a dwell time of 10 s. Subsequently, HPT processing was carried out at a rotation speed of 1 rpm, followed by another 10 s dwell period before unloading. Finally, the deformed samples were stored at 253 K to reduce strain relaxation.

For Vickers hardness tests, the sample surfaces were ground by a standard metallographic preparation, reaching a 4000-grit surface quality using SiC papers. The samples were then subjected to Vickers indentation under a load of 500 g and a dwell time of 10 s. Nanohardness and Young's modulus were determined via nanoindentation, employing the continuous stiffness measurement mode with a Berkovich indenter. A standard sample of fused silica was used for calibration and the indenter elastic deformation was included by calibration. A load rate of 10 nm s^{-1}, an indentation depth of 200 nm, and at least 220 effective points were averaged for Young's modulus estimation on the 10 rotation HPT-processed CoCrFeNi alloy (see details in Appendix E). This ultimately produces a Young's modulus of about 227 GPa, which closely matches the real case because of the standard sample calibration.

Two samples were used for X-ray diffraction (XRD) measurements. XRD measurements were performed on the same sample surface at different deformation states and at different sample depths. The deformed surface did not undergo any additional mechanical processing, such as grinding or polishing. XRD was carried out using a Siemens D5000 diffractometer employing Cu-Kα radiation. Beam scanning involved Bragg-Brentano geometry and a step size of 0.02° with an integration time of 16 s, while rotating the sample stage. Calibration was performed under the same settings using SiO_2 powder. The lattice parameter (a) was calculated using the formula: $a = d\sqrt{h^2 + k^2 + l^2}$, where d is the interplanar spacing, and (hkl) are the Miller indices. The size of the coherently scattering domains was estimated by the Williamson–Hall (W–H) method, $\beta_{hkl} \cos\theta = 0.89\lambda/D + 4\varepsilon \sin\theta$, with the corrected full width at half maximum (FWHM) of the (hkl) reflections, β_{hkl}, Bragg angle, θ, wavelength, λ, domain size, D, and micro-strain, ε. In the W–H plot, the intercept (*Int.*) and its error ($Int._{err.}$) can be provided. The average domain size (D) can then be calculated and the associated error was determined using formula $D \times (Int._{err.}/Int.)$. The dislocation densities (ρ) were estimated and further averaged by the methods of domain size ($\rho = 3/D^2$) and micro-strain ($\rho = k\varepsilon^2/(Fb^2)$), for FCC materials, k is assumed as 16.1, the interaction factor F is assumed to be 1, and b is the Burgers vector [15–17].

Misorientations were determined through electron backscatter diffraction (EBSD) employing an EDAX detector. To improve the quality of the sample surface, a final polishing step with oxide polishing suspension (OPS, 40 nm particle size) was performed before EBSD measurements, and the evaluation of EBSD maps was processed by the EDAX orientation imaging microscopy (OIM) software. For EBSD data collection, EBSD scan step sizes of 0.1 and 0.05 μm were applied for all the strained microstructures, except for the homogenized state, which was scanned with a step size of 1 μm to reduce image drift over a large map dimension. For EBSD data processing, data points with a confidence index lower than 0.1 were omitted. Additionally, twin boundaries (TBs) were defined by Σ3 <111> and Σ9 <110> with a tolerance of 1°. A color-coded map with the indicated transverse direction (TD) and the rolling direction (RD) was used for all EBSD maps.

Transmission electron microscopy (TEM) specimens were electro-polished using an electrolyte composed of methanol (70 vol.%), glycerine (20 vol.%) and perchloric acid (10 vol.%) employing a twin-jet polisher (Struers Tenupol-5) at 248 K and a voltage of 19 V. TEM was performed with an image-corrected FEI Titan Themis 60-300 microscope equipped with a high brightness field emission gun (XFEG), a monochromator, a quadrupole energy-dispersive X-ray spectroscopy (EDS) system, a high angle annular dark field (HAADF) detector (Fischione Model 3000) and a fast CMOS camera (Ceta, 4k × 4k). The microscope was operated at 3.45 kV extraction voltage and 300 kV acceleration voltage. In addition, grain size distributions were statistically calculated by 320 grains from multiple dark field (DF) images.

Strain analyses were conducted using nanobeam diffraction patterns (NBDPs) [18,19] and a commercial version of the geometric phase analysis (GPA) [20] software (GPA Phase 2.0, HREM Research, www.hremresearch.com), which is implemented in Digital Micrograph as a plug-in. NBDPs were acquired in μ-probe mode using parallel illumination, whereas aberration-corrected high-resolution TEM (HRTEM) images were used as input for the GPA to assess local strains within the nanograins. The strain energy stored in the HPT-processed material was estimated by the GPA, and further verified by the heat release upon heating using differential scanning calorimetry (DSC, Mettler Toledo DSC 3) measurements with heating rates of 3 and 5 K min^{-1}, respectively.

3. Results

3.1. Hardness evolution

During HPT deformation, the simple (geometric) torsional shear strain (γ) imposed on the sample is approximately given by the relationship $\gamma = 2\pi rN/t$ [3,21,22], with the distance from the rotation axis, *r*, the number of rotations, *N*, and the thickness of the sample after HPT processing, *t*. Fig. 1(a) shows the variation of hardness along the radius of the samples by the different numbers of HPT rotations. Each data point was calculated by four equivalent positions, as depicted in the inset in Fig. 1(b). One can see in Fig. 1(a), the homogenized state shows the lowest hardness of about 1.1 GPa. A significant increase was observed in hardness from the center to the outer edge after pure compression, which is attributed to the plastic flow along the radial direction. The anvils created a certain amount of extrusive force due to their geometric constraint, resulting in material plastic flow from the center to the edge of the sample during compression (see Appendix A). A similar trend was observed for different HPT rotations, and the hardness reached a plateau of about 4.6 GPa after 10 rotations of HPT.

Fig. 1(a) displays that the hardness at the center of the samples with zero shear strain exhibits an increase from the homogenized state to the state after 10 rotations. This can partially be attributed to the connectivity of grains along the radial direction as explained in the following. In the early stages of deformation, a slight increase of hardness at the center was achieved by pure compression. During HPT processing, grains experienced varying shear strains from the edge to the center, and severe fragmentation of grains occurred near the edge. However, the connectivity of grains, i.e. GBs, contributed to the gradual grain fragmentation from the largest strain region (edge) to the zero strain region (center). Meanwhile, grains at the sample center were gradually refined with continuous rotations and formed an increased hardness at the centers.

Fig. 1(b) exhibits the hardness variation as a function of shear strain. A rapid transition in the evolution of hardness is noticed during 0.25 and 1 rotations of HPT processing, followed by a hardness plateau after a shear strain of 36.7 marked in Fig. 1(a), indicating the entire hardening process is finalized at this strain level.

3.2. Microstructural evolution

3.2.1. XRD measurements

XRD patterns from the homogenized and deformed samples in Fig. 2 (a) indicate a single FCC phase in CoCrFeNi alloys. The lattice parameter ($\overline{a}$) was determined by averaging the values from five reflections for the individual deformation states. It was observed that the lattice parameter exhibited an increasing trend with an increase in HPT rotations, revealing lattice distortions after deformation. Besides, one can see a strong (111) texture was created after 0.25 rotations, and the correlated hardness showed a sharp increase in Fig. 1(b). Therefore, the (111) texture formation contributing to the hardness improvement is suggested during HPT processing. This result is in good agreement with studies indicating that the (111) texture yields the highest hardening effect among all the textures of FCC-structured metallic materials [23, 24].

The peak broadening in Fig. 2(a) indicates that grains were refined after deformation. Fig. 2(b) displays a significant increase in FWHM of the (111) reflection from 0.25 to 10 rotations and rather constant values of the FWHM between 10 and 20 rotations. This observation indicates a decrease of the size of coherently scattering domains from 0.25 to 10 rotations and the occurrence of a steady state with minimum grain size after 10 rotations. Meanwhile, a decrease of the Bragg angle of the (111) reflection after 0.25 rotations was observed, implying an expansion of the interplanar spacing of the (111) planes due to lattice distortions, thus leading to an increase in the strain energy.

Fig. 3(a) shows the size of the coherently scattering domains and the dislocation density as a function of the number of HPT rotations. The domain size rapidly decreased with increasing HPT rotations, and the dislocation density increased to about 10^{16} m^{-2} when reaching the hardness saturation after 10 rotations, in Fig. 1.

3.2.2. Microstructure distributions after hardness saturation

To reveal the microstructural states after 10 rotations of HPT processing, in Fig. 3(d), the domain size along the normal direction (ND: along the axial direction of the sample) and the grain size along the transverse direction (TD: along the radial direction of the sample) were evaluated by XRD and TEM methods, respectively. The domain size distributions along the ND were obtained at different sample depths, as shown in Fig. 3(b). The top surface of the sample presented the smallest value because of the direct contact with the anvil (holder) during HPT processing, and the most severe grain fragmentation occurred in the contact regions. A slight increase in the domain size from the top to the center of the sample suggests a gradient in grain fragmentation along the ND. If the hardness measurement would have been performed along the ND, a slight decrease in hardness is expected from the top to the center based on the Hall-Petch relationship [25]. However, the difference could be ignored due to the small deviations in the domain size along the ND, and the microstructures in terms of the domain size along the ND can be

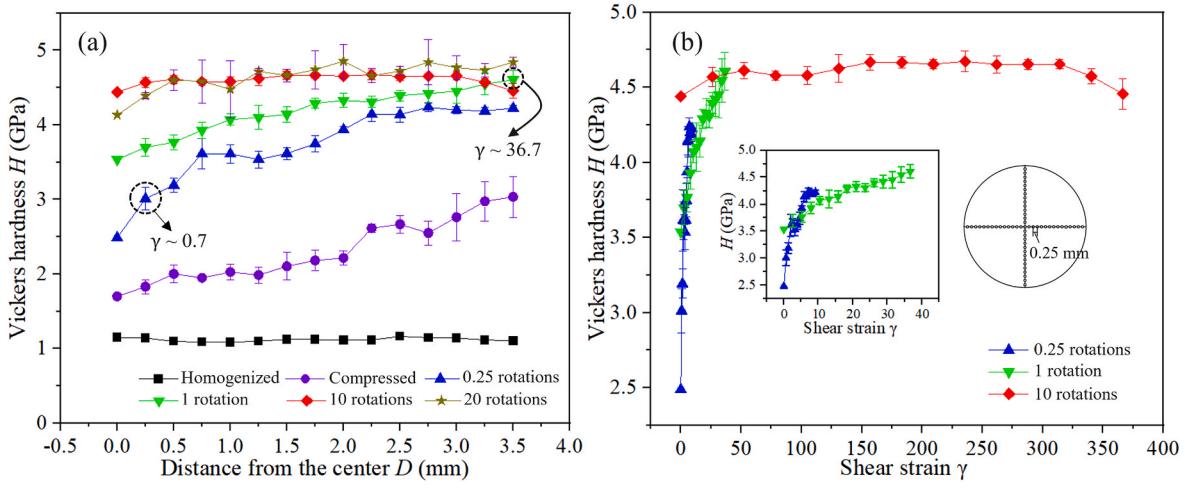

Fig. 1. (a) Hardness evolution after different numbers of HPT rotations plotted against the distance from the sample center. (b) Hardness evolution as a function of shear strain. Insets are the close-up of the hardness evolution after 0.25 and 1 rotation HPT processing and a map displaying the positions of the Vickers indentations on the sample.

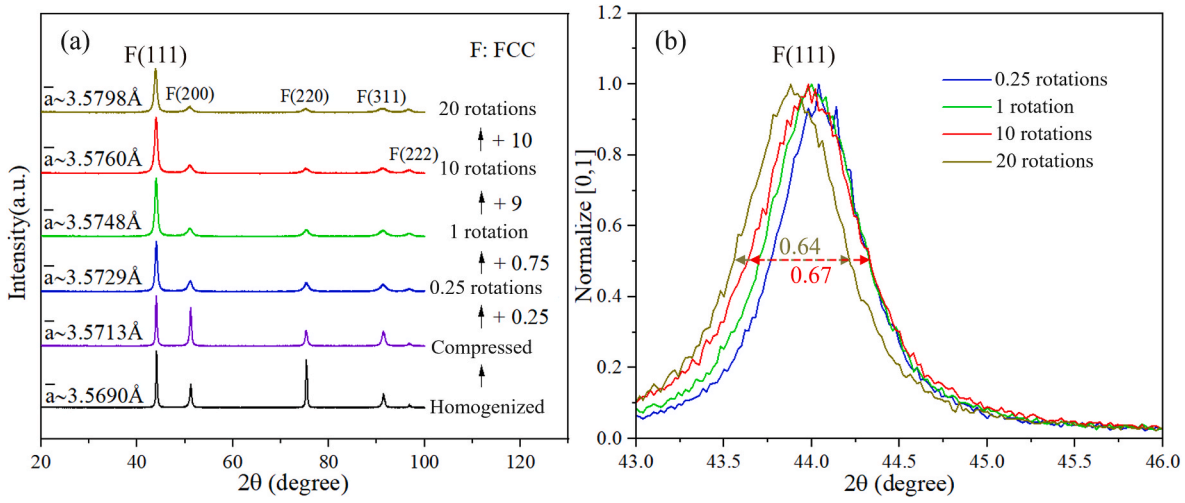

Fig. 2. (a) XRD patterns of the CoCrFeNi alloy showing the states after homogenization and after deformation, (b) displaying the evolution of the normalized (111) reflections after 0.25, 1, 10, and 20 rotations, and the rather constant FWHM values between 10 and 20 rotations.

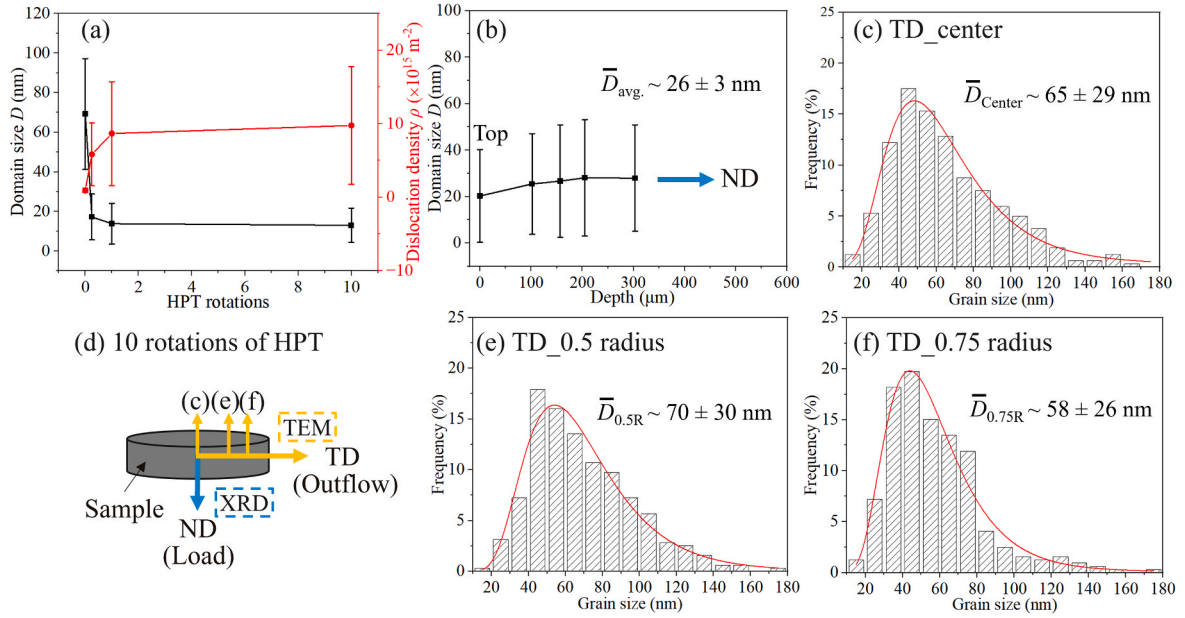

Fig. 3. (a) The variations of domain size and dislocation density as a function of the number of HPT rotations (the data was measured across the entire region of a single sample surface; HPT with zero rotations denotes pure compression). (b) The domain size distributions on another sample obtained by XRD along the ND in (d). The grain size distributions obtained via TEM (c, e, f) along the TD in (d), and the grain size distributions were fitted by log-normal functions in the different regions, i.e. center, 0.5 radius, and 0.75 radius.

regarded as homogeneous.

The grain size distributions along the TD after 10 rotations are displayed in Fig. 3(c, e, f), i.e. center, 0.5 radius, and 0.75 radius. The averaged values of the grain size in these regions are very similar, indicating a steady-state of the grain size along the TD after 10 rotations. The grain size measurements via TEM yielded somewhat larger values than the domain sizes estimated by XRD, primarily due to the differing sensitivities of XRD and TEM concerning small orientation differences [26,27]. Consequently, nearly homogeneous microstructures of the entire sample were achieved after 10 rotations.

3.2.3. EBSD measurements

Fig. 4(a) shows the inverse pole figure map of the homogenized CoCrFeNi alloy, with an estimated grain size of about 90 μm using the line intercept method. A high fraction of high-angle grain boundaries (HAGBs: marked in blue) was observed after homogenization. In an early-stage deformation with a shear strain of 0.7, Fig. 4(b), numerous TBs and LAGBs formed. With continued straining, grains were severely fragmented at a shear strain (γ) of about 39.3, as shown in Fig. 4(c). As well known, a decreased fraction of LAGBs is expected after large deformation of conventional materials [28–30]. However, an anomalously high density of LAGBs with a fraction of about 80 % was achieved at a strain of 39.3, and the newly-formed LAGBs (marked in red) are displayed in the magnification from Fig. 4(c). LAGBs appear to significantly contribute to the increase in hardness, since the hardness close to this strain level already reached its maximum value (or saturation), see the hardness at a shear strain (γ) of about 36.7 in Fig. 1(a).

The misorientation distributions in Fig. 4(d) show that a large number of LAGBs and TBs, which are commonly regarded as low-energy GBs, formed after deformation. It has been proposed that the formation

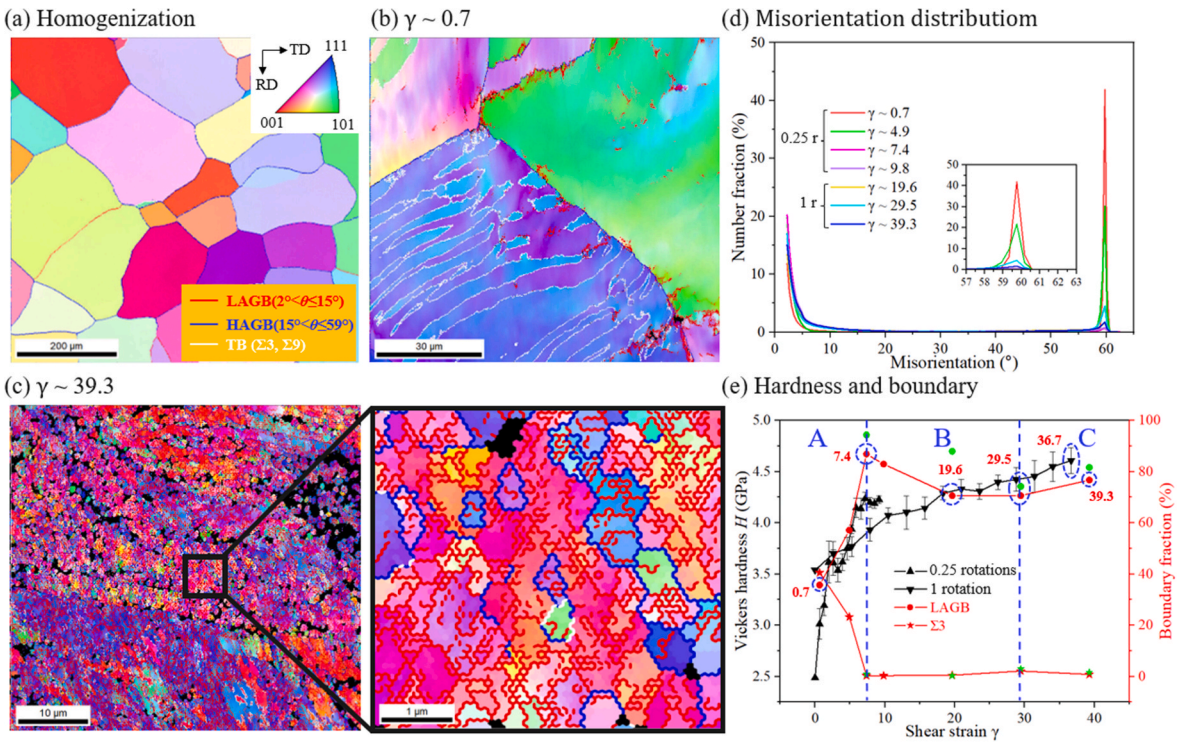

Fig. 4. EBSD results of CoCrFeNi alloys: (a) the homogenized sample showing an average grain size of about 90 μm, and the GB specification for all EBSD maps, LAGB (red: $2° < \theta \leq 15°$), HAGB (blue: $15° < \theta \leq 59°$), TB (white: Σ3, Σ9); (b) detail showing deformed grains at a shear strain $\gamma \sim 0.7$; (c) detail showing deformed grains at a shear strain $\gamma \sim 39.3$, and the corresponding close-up with a high fraction of LAGBs; (d) misorientation distributions plotted for different shear strain levels from samples after 0.25 rotations (0.25 r) and 1 rotation (1 r) HPT processing, and the fractions of misorientation angles greater than 63° are zero; (e) Vickers hardness (both 0.25 and 1 rotations consideration aim to reach a general case) and boundary fraction as a function of shear strain, therein, the red and green data was acquired with EBSD scan step sizes of 100 nm and 50 nm, respectively. (For interpretation of the references to color in this figure legend, the reader is referred to the Web version of this article.)

of low-energy boundaries contributes to structural refinement at a finer scale [31], which can be verified by the rapid decrease in domain size shown in Fig. 3(a). Thus, grain refinement should be closely related to low-energy boundaries, namely, LAGBs and TBs that play an important role in the evolution of hardness of the CoCrFeNi alloy.

The variations in the fractions of LAGBs and TBs as a function of shear strain are exhibited in Fig. 4(e), and the directly correlated hardness variations from the inset in Fig. 1(b) was combined. One can see that the fraction of TBs decreases rapidly to nearly zero, while the fraction of LAGBs presents a similar tendency to the variation of hardness in the strain range from 0.7 to 36.7. It thus can be speculated that the variation in hardness is dominated by the variation of LAGB fraction. As a LAGB can be considered as an array of individual dislocations [32, 33], the higher fraction of LAGBs suggests a higher dislocation density (or hardness), which was verified by the high dislocation densities obtained from the estimation based on XRD, Fig. 3(a), providing a rationale for the strong impact of the fraction of LAGBs on the hardness.

However, the dependence of the hardness on the fraction of LAGBs does not hold over the entire hardening process. A decrease of the LAGB fraction from a strain of 7.4 to 19.6 accompanying an increase in hardness was observed after 1 HPT rotation, see Fig. 4(e). Other hardening mechanisms were activated in the above strain range and thus a strain range from 0.7 to 7.4 was considered. Taking into account the individual rotation, in Fig. 4(e), a significant increase in hardness was seen after 0.25 and 1 rotations, respectively. Consequently, a LAGB-dominated hardness increase is indicated for the strain range between 0.7 and 7.4, i.e. in stage (A). It should be noted that different hardness values were observed for the various samples at equivalent strain levels, as shown in Fig. 4(e) at strains ranging from 0.7 to 7.4. These discrepancies were inevitable due to the initially differently oriented grains prior to deformation; an example of the as-deformed sample is shown in Fig. 4(a). Since hardness is affected by different orientations [34], the initial coarse grains were not completely refined by the relatively low strain in the early stages of deformation, resulting in significant hardness variations.

A sharp decrease of the TB fractions from a strain of 0.7 to 7.4 is shown in Fig. 4(e). This occurrence is likely associated with the effect of detwinning, a process that removes the pre-existing twins through mechanisms such as dislocation-twin interactions [35]. A rapid increase in dislocation density from pure compression to 1 HPT rotation was observed (see Fig. 3(a)), which suggests a strong interaction between dislocations and twins, leading to twin annihilation. This process implies an interesting feature for further systematic analyses and/or simulation studies. With further straining, reduced fractions of LAGBs from 86.8 % ($\gamma \sim 7.4$) to 70.6 % ($\gamma \sim 19.6$) were observed, indicating that the increase in hardness after stage (A) is a result of HAGBs, since the fractions of TBs is close to zero in that deformation stage.

3.2.4. *TEM observations*

Following the analyses of stage (A) in Fig. 4(e), an increase of the fraction of HAGBs is inferred. The hardening process appears to be governed by GB strengthening, and the grain size distributions were thus calculated at different strain levels. As presented in Fig. 5, the grain size was estimated to be (80 ± 30) nm and (54 ± 23) nm at a strain of 19.6 and 29.5, respectively. Therein, the grain size at a strain of 29.5 is very close to the HPT-processed sample with 10 rotations, see Fig. 3(c, e, f). It is worth noting that the grain size already reached its minimum value at a strain of 29.5, suggesting GB saturation. The increase in the fraction of HAGBs is attributed to the transformation of LAGBs under continued straining. HAGBs contributing to the hardness improvement are thus proposed after a strain of 7.4 in Fig. 4(e).

In addition, it should be pointed out that the data plotted by red

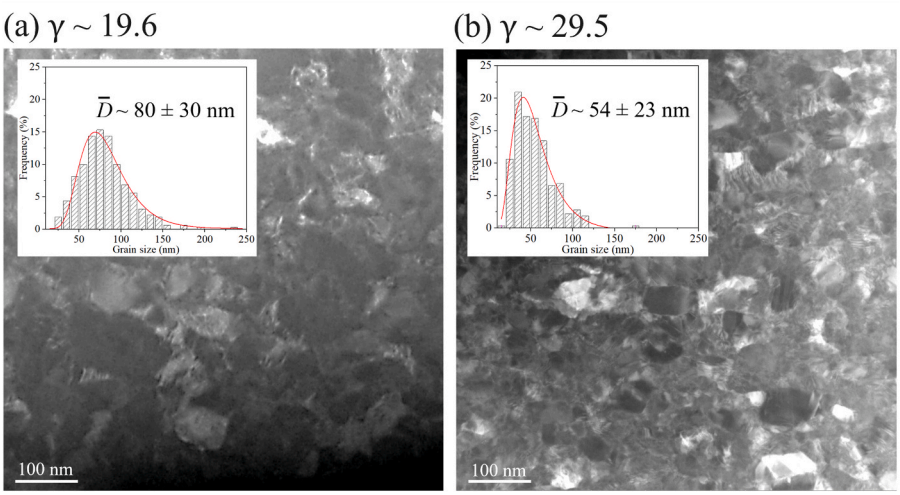

Fig. 5. HAADF images and the statistical log-normal distribution of grain sizes at shear strains (a) γ ~ 19.6 and (b) γ ~ 29.5.

points in Fig. 4(e) was acquired by applying an EBSD scan with a step size of 100 nm, which was larger than the grain sizes at the strain of 19.6 and 29.5. The green points obtained with a step size of 50 nm present higher fractions of LAGBs than the data obtained with a step size of 100 nm due to the step size dependence of the resolution. However, both step sizes yielded similar variations of the abundances of LAGBs and TBs, showing very little influence of the step size on the EBSD results. As mentioned above, GB saturation was achieved at a strain of 29.5, indicating that the entire grain refinement process or GB strengthening was completed at this strain level. Therefore, a dominance of HAGB-related hardening is indicated for stage (B) of the observed HPT straining.

However, the hardness is not yet saturated at a strain of 29.5. A subsequent increase in hardness was observed until saturation, i.e. γ ~ 36.7, in Fig. 4(e). This suggests the presence of additional hardening mechanisms after GB strengthening, and the hardening effects should be generated in the grain interior since the intergrain contributions were achieved by the GBs. The hardening process after the strain of 29.5 was thus identified as an independent stage (C).

To reveal the hardening mechanisms after GB strengthening, the microstructures at a large strain of about 295 were analyzed using HRTEM, as shown in Fig. 6. The local region (A) depicts that dislocation slip induced the formation of stacking faults (SFs) and nanotwins. A similar case was observed in nanocrystalline copper, where nanotwins nucleated heterogeneously at GBs and grew into the grain interior via partial dislocation emission from the GB [36]. The generation of SFs and nanotwins in region (A) suggests a high probability of dislocation emission from the GBs. A growth twin was observed in the local region (B), where a strained GB with a discernible shape change was found [37]. The formation of a growth twin appears to be induced by the strained GB, since GBs with kinks create strain, and the various kink angles promote twin formation [38,39]. Trailing the region (B), nanotwins were observed in the region (C), as well as in the region (D), which were verified by the fast Fourier transform (FFT) images shown as inserts in Fig. 6. In addition, multiple SFs contribute to the twin growth, as displayed for region (D). Twins are prominent within the nanograin after hardness saturation. It is known that TBs play an important role in strengthening through impeding dislocation motion [40,41]. The observation of numerous twins inside the nanograin suggests that the

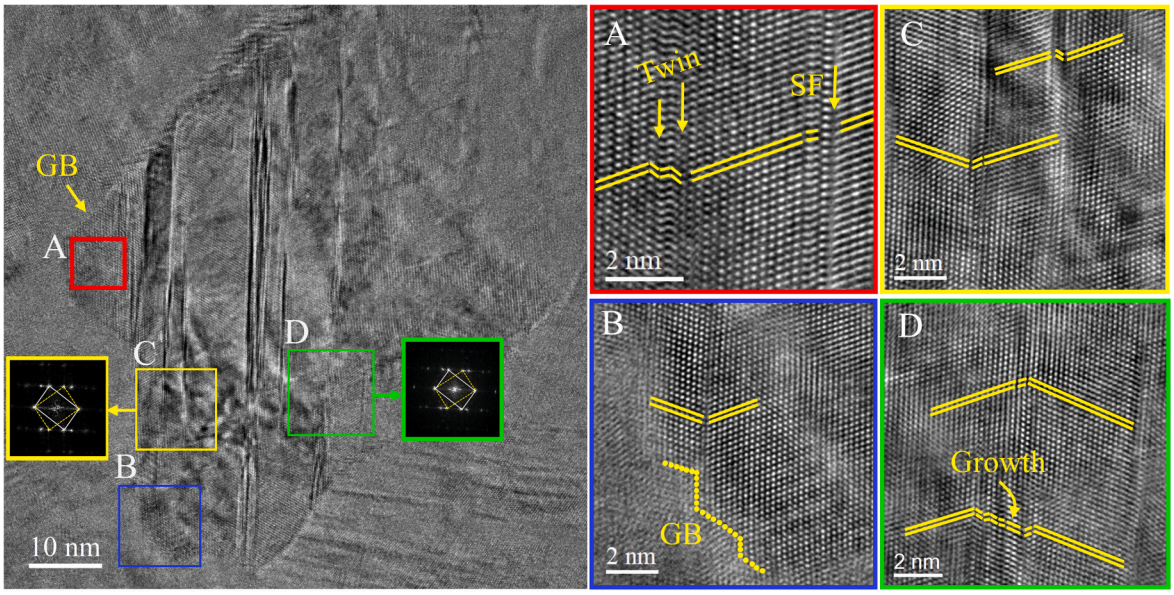

Fig. 6. HRTEM image obtained after applying a shear strain of γ ~ 295. (A) Nanotwins and SFs; (B) strained GB (yellow dots) and nanotwin; (C) and (D) nanotwin regions, as well as the corresponding FFT patterns. (For interpretation of the references to color in this figure legend, the reader is referred to the Web version of this article.)

dislocation motion was severely hindered by the TBs, leading to an increase in hardness. The twin-dominated hardening process was thus identified as the dominant hardening mechanism in stage (C).

Additionally, considerable SFs were created within the nanograins during straining. An extension of ductility by the generation of SFs [42,43] or through the gliding of SFs along TBs [41,44,45] has been reported. Consequently, a saturation in hardness was reached due to the continued creation and interaction of dislocations, SFs, and twins within the nanograins.

Fig. 7 shows the defect evolution in a nanograin after applying a shear strain of about 295. It is well-known that a full dislocation is characterized by a Burgers vector of $\boldsymbol{b}_1 = a/2\langle 110\rangle$ in the slip planes of an FCC structure, and a Shockley partial dislocation is generally specified by a Burgers vector of $\boldsymbol{b}_2 = a/6\langle 112\rangle$, where a is the lattice constant. Therefore, a correlation of the full dislocation to the Shockley partial dislocation can be presented by the ratio of their absolute values, i.e. $|\boldsymbol{b}_1|/|\boldsymbol{b}_2| = \sqrt{3}$. As observed in the close-up of region (A), the magnitude of a full dislocation can be measured by the profile from a to b, i.e. about 0.228 nm, and the shift in stacking positions resulting from the glide of the partial dislocation was about 0.13 nm. Consequently, the ratio of a full dislocation to a partial is about 1.75, which is very close to the normal value of $\sqrt{3}$. This result confirmed the presence of a Shockley partial dislocation in region (A).

Fig. 6 illustrates that twin growth in region (D) was initiated by multiple SFs. In region (A) of Fig. 7, a nanotwin with a thickness of a single atomic layer was formed by a Shockley partial dislocation, which is consistent with the deformation twins that are typically formed by $a/6\langle 112\rangle$ Shockley partial dislocations [46]. As it appears that nanotwins originated from a single SF, a single Shockley partial dislocation is referred to as a single-layer twin in this study. Trailing the region (A), a partial dislocation was formed as illustrated by the Burgers circuit in the local region (B) and further a SF was observed. Importantly, the thickness of the twin ($D_t \sim 0.34$ nm) is larger than the separation distance of the SF ($D_s \sim 0.28$ nm). Both of them were subjected to tensile strains since the magnitude of full dislocations with zero strain amounts to 0.228 nm, suggesting that the strain and stress concentrations near the twin were higher than near the SF. The twin trails a SF behind and was ultimately stopped at the SF during the propagation of Shockley partial dislocation. The process of twins trailing SFs also can be elucidated as the gliding of dislocations, wherein the displacement of atom stacking positions decreased along the direction of propagation of the Shockley partial dislocation, resulting in the nanotwin ending at a SF.

3.3. Strain analyses

Introducing low-energy boundaries into nanoscale structures is a challenge for the improvement of material properties [47], especially concerning the generation of TBs at the nanoscale [41]. However, high densities of low-energy configurations, i.e. LAGBs, TBs, and SFs, were frequently observed in fine-grained CoCrFeNi alloys after deformation, as shown in Figs. 4, 6 and 7. To further investigate the evolution of microstructures, which are closely related to the internal strains, strain fields within nanograins were analyzed using the GPA and NBDP methods.

As depicted in Fig. 7 (b), strain fields in the same grain (Fig. 7 (a)) were determined by the GPA method, which can calculate strain values for each pixel [20,48]. The regions outside the grain were masked by gray color, since those were not relevant for quantitative strain analyses in the grain interior. In Fig. 7(b), the distribution of ω_{xy} presents the non-uniform distribution of defect debris inside the grain, as exemplified by the white arrows. Notably, there were considerable regions characterized by either very high or very low values of ω_{xy}, revealing a heterogeneous distribution of defects in the grain interior, and these regions were deliberately avoided in the present analyses. It should be noted that no precipitation was found in the present sample, which was evidenced by the uniform element distributions obtained from the EDS measurements shown in Appendix B.

To illustrate the influence of deformation-induced low-energy configurations on the nanograin, the profile of ω_{xy} along the nanotwin, marked as a white dashed box in Fig. 7(b), was acquired. The variation in ω_{xy} from c to d displays a slight deviation of 1.3° in rotation angles, revealing that the grain was bent. The emission of Shockley partial dislocation in region (A) appears to be revealed by the deformed nanograin, i.e. grain bending. As a result, twins were formed in the

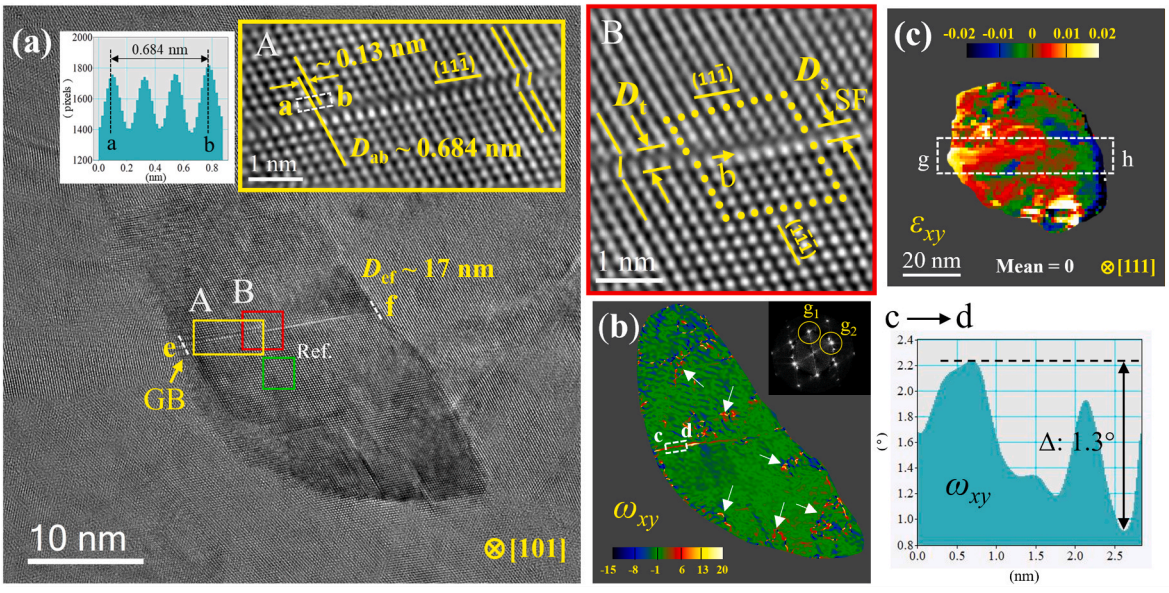

Fig. 7. (a) HRTEM image after applying a simple (geometric) torsional shear strain of $\gamma \sim 295$: (A) Shockley partial dislocation with a single-layer twin, and the corresponding intensity profile from the atomic columns a to b; (B) the Burgers circuit with a vector of **b**, which is seen between a twin and a SF. (b) Distribution of the relative rigid-body rotation component obtained by GPA, the lattice vectors $\mathbf{g_1}$ and $\mathbf{g_2}$ were used for strain tensor calculation, the green square region in (a) served as reference. The masked in-plane rigid-body rotation map ω_{xy} ($\omega_{xy} = 1/2(\varepsilon_{yx} - \varepsilon_{xy})$, anti-clockwise positive) with defect debris marked by white arrows, and the corresponding profile from c to d. (c) Strain analysis using the NBDP method for a different (111)-oriented nanograin and the resolved shear strain distribution ε_{xy}. (For interpretation of the references to color in this figure legend, the reader is referred to the Web version of this article.)

nanograin interiors during the propagation of Shockley partial dislocations, further contributing to the hardening effects in stage (C).

It has been well accepted that the formation of deformation twins proceeds via the emission of Shockley partial dislocations from GBs in nanograins [39], however, the twinning process has not been experimentally verified in nanocrystalline CoCrFeNi alloys. As mentioned above, in region (B) a larger separation distance in the twin (D_t) than the SF (D_s) reveals decreased strain and further implies that the Shockley partial dislocation was emitted by the GB, which is located in the region e in Fig. 7(a). To present a more representative case due to a strong (111) texture formation after deformation, a different (111)-oriented nanograin with a size of about 60 nm was chosen for strain analyses. The NBDP as a robust method for the local strain evaluation in one single nanograin was conducted, and the detailed calculation can be found in Appendix C.

The shear strain (ε_{xy}) distribution calculated by the NBDP method is shown in Fig. 7(c). Clearly, the strain distribution in the grain interior is strongly non-uniform, and the observed shear strain discontinuities indicate the presence of defect debris in the grain interior. It is important to note that a higher concentration of ε_{xy} was observed at the GB than in the grain interior (see the region g to h), indicating that the Shockley partial dislocations or nanotwins primarily emerged from GBs.

4. Discussion

Vickers hardness tests were performed on different deformation states of CoCrFeNi alloys, and the corresponding microstructures were systematically investigated by XRD, EBSD, and TEM. During HPT processing, multiple deformation processes were activated before reaching hardness saturation ($\gamma \sim 36.7$ in Fig. 1(a)). The hardening mechanisms for the different stages in the hardness evolution are now discussed. After the hardness saturation, the critical stress for twin nucleation is estimated, and the stability of the microstructure as well as the capacity of strain storage are further discussed.

4.1. Deformation mechanisms

Hardness variation is closely related to the microstructural evolution, and the sequence of deformation mechanisms of CoCrFeNi alloys during HPT processing is discussed. It is known that large strain deformation induces the activation of GB-mediated and twinning mechanisms in CoCrFeNi-based HEAs [49,50]. In a macroscopic sense, a three-stage hardening mechanism is suggested for the present CoCrFeNi alloy: LAGB-dominated hardening (σ_L) in stage (A), HAGB-dominated hardening (σ_H) in stage (B), and twin-dominated hardening (σ_T) in stage (C), Fig. 4(e), expressed as:

$$\sigma_{total} = \sigma_L + \sigma_H + \sigma_T \quad (1)$$

In the early stages of deformation, dislocation activity-dominated deformation has been proposed by Wang et al. [9], and it occurs below a strain of 0.4 in CoCrFeNi alloys. With further straining ($\gamma < 0.7$), the twinning process is activated due to grain interactions [51]. As expected, a high fraction of TBs with about 40.4 % at a strain of 0.7 was estimated, Fig. 4(b, e).

Subsequently, the twin annihilation process was activated at strains higher than 0.7, as shown for stage (A) in Fig. 4(e). As a high density of dislocations has been created at a strain of 0.4 [9], the twin annihilation is most probably attributed to a detwinning process, which was initiated by the dislocation-twin interactions [35]. It should be noted that the sharp increase in hardness from a strain of 0.7 to 7.4 accompanying the increased fractions of LAGBs and the decreased fractions of TBs suggests that the hardening process in stage (A) is dominated by the contribution from LAGBs.

The high density of dislocations offers favorable conditions for LAGB formation. Dislocations accumulated and self-organized into LAGBs [10], and an increase in the fraction of LAGBs is a result of the increased dislocation density, further contributing to a high value of hardness, stage (A) in Fig. 4(e). Meanwhile, a similar scenario with a higher fraction of LAGBs accompanying a higher strength was reported [52], revealing LAGB-dominated hardening (σ_L) in stage (A).

In stage (B), the hardness exhibits a continuous increase accompanying the annihilation of LAGBs. It can be inferred that there is an increase in the fraction of HAGBs with an extremely low fraction of TBs, since most of the special GBs were LAGBs, HAGBs, and TBs from EBSD processing. These observed TB variations agree well with the suggestion that the abundant twinning activity in the coarse-grained material is strongly inhibited by grain refinement [53], and TB formation also becomes difficult as the twin nucleation stress increases with decreasing grain size [54].

As indicated in Fig. 5, the grain size was refined to the nanoscale after HPT processing, with pronounced grain size variations ($\gamma \sim 19.6$, (80 ± 30) nm; $\gamma \sim 29.5$, (54 ± 23) nm). Grain refinement occurs in stage (B), and is completed at a strain of about 29.5, since the average grain size reached the minimum of 54 nm at that strain, as compared with the grain sizes after 10 rotations in Fig. 3 (c, e, f). The scaling of the hardness with grain size (i.e. the Hall-Petch strengthening) has been extensively investigated [6,25,55,56]. In the present work, the highest density of GBs was achieved after grain refinement reaching the minimum size and the additional transformation of LAGBs into HAGBs by the absorption of dislocations at GBs [57]. These two effects lead to an increase in the fraction of HAGBs. Consequently, dislocation motion is severely impeded by HAGBs, and an increase in hardness is obtained, resulting in HAGB-dominated hardening (σ_H) in stage (B).

In stage (C), an increase in hardness is accompanied by a slight increase in the fraction of LAGBs. It can be inferred that the fraction of HAGBs simultaneously decreases, since the fraction of remaining twins is close to zero. However, the increased hardness in stage (C) is actually not dominated by GBs. As mentioned in stage (B), the grain size obtained from TEM investigations reveals a minimum value at a strain of about 29.5 ($\sim$ 54 nm), and the hardening effect resulting from GB strengthening is completed at that strain, that is, the density of GBs has been saturated at this strain level. Additionally, the contribution of LAGBs to strength is also comparable with that of the HAGBs [43,58], indicating the enhanced hardness is no longer dominated by GBs in stage (C). GB-mediated plastic deformation might be suppressed by the inherent atomic configurations along GBs, shifting the dominating deformation mechanism to partial dislocation emission from GBs at the smallest grain sizes [59].

At a grain size of about 50 nm, Zhu et al. proposed that partial dislocation emission from GBs with the formation of twins tends to be a dominant deformation process [60]. As expected, numerous partial dislocations accompanying twins and SFs in the nanograin interior were observed, Fig. 6, and thus SFs and twins within nanograins play a major role in the evolution of hardness after GB saturation. SFs tend to increase plasticity, as reported SF-induced plasticity in HEAs [42], while numerous twins contribute to the increase of hardness because they present very effective barriers to dislocation motion [61], and twin-dominated hardening (σ_T) in the nanoscale grains was thus proposed in stage(C).

It is well-established that the nucleation of partial dislocations is preferred at GBs [42]. In this context, the high density of GBs after grain refinement offers favorable conditions for partial dislocation emission, leading to numerous twins and SFs within nanograins. This interpretation is supported by the NBDP results in Fig. 7(c), which reveals a high strain concentration along the GB. This situation favors the emission of partial dislocations from GBs into the grain interior. As displayed in Fig. 6, numerous twins were observed within a nanograin. The high density of nanotwins confines dislocation movement [62,63], contributing to an increase in hardness in stage (C). Meanwhile, single-layer nanotwins trail SFs behind during the propagation of partial dislocations, region (B) in Fig. 7. Considerable amounts of SFs, which might

tend to promote the extension of ductility [41–45], were created during straining. As a result, a saturation in hardness was reached due to the concomitant contributions of SFs and twins within the nanograins.

4.2. Critical stress for twin nucleation

A high density of twins gives rise to a high strength, the twin nucleation thus serves as an important contributor for the strengthening process that occurs in stage (C). Various models for twin nucleation have been proposed, including the pole mechanism [64], the double-cross-slip mechanism [65], and others [66]. In the present CoCrFeNi alloy, a strong tendency to form nanotwins would be given through the double-cross-slip mechanism, since the $a/6\langle 112\rangle$ Shockley partial dislocation was evidenced gliding on a {111} plane (the region (A) in Fig. 7). This observation presents a crucial feature after dislocation dissociation for the double-cross-slip model [67]. According to Ref. [67], the stress required for twin nucleation can be expressed as follows:

$$\sigma_c = \frac{2\alpha\mu b_p}{D_{ef}} + \frac{\gamma_{sf}}{b_p} + \tau_p \tag{2}$$

where μ is the shear modulus (84 GPa [68]), $\boldsymbol{b}_\mathrm{p}$ is the Burgers vector of the Shockley partial dislocations, D_ef represents the length of the dislocation source, γ_sf is the SFE, τ_p denotes the Peierls stress, and α is a constant equal to 0.5 for an edge dislocation or equal to 1.5 for a screw dislocation [43,46], respectively. Therein, the Burgers vector is determined by the lattice constant of the material after 10 HPT rotations, see Fig. 2(a), i.e. $|\overline{a}| = 0.3576$ nm, $|b_p| = |\overline{a}|/\sqrt{6}$, $|b_p| \sim 0.146$ nm.

The length of the dislocation source, D_ef, is estimated to be about 17 nm, Fig. 7(a). Moreover, the specified vector (b) in the Burgers circuit (the region (B) in Fig. 7) is parallel to the dislocation source, suggesting a screw dislocation for the dislocation source, and α is thus considered as 1.5.

In Eq. (2), the first term represents the minimum stress required to create a half-loop of the fault or to initiate twin nucleation [67]. The last two terms, i.e. $\gamma_{sf}/b_p + \tau_p$, associated with the SFE and the Peierls stress are independent of the dislocation source [46], and could be disregarded. Therefore, the critical stress for twin nucleation, about 2.16 GPa, is ultimately determined. This value closely agrees with the nucleation stress estimated for single-phase FCC CoCrNi alloys (~ 2.24 GPa [46]), and the twinning process is difficult to be activated in nanocrystalline CoCrFeNi alloys, except as the imposed stress is higher than 2.16 GPa.

4.3. Stability of microstructures

It is known that the evolution of defect structures of metallic materials during deformation is closely related to its SFE [69]. A face-centered cubic to hexagonal close-packed phase transformation has been reported in pure Nickel [70] with high SFE (~ 127.37 mJ m^{-2} [71]) and CoCrFeNiMn [72] with low SFE (~ 21 mJ m^{-2} [73]) after deformation. However, during the deformation of CoCrFeNi alloys (~ 32.5 mJ m^{-2} [74]), the SFE of which falls between pure Nickel and the CoCrFeNiMn alloy, no phase transformation has been found for the current alloy, revealing a high stability of the FCC phase in CoCrFeNi alloys.

As observed in Fig. 4(e), high fractions of LAGBs were formed after stage (A) ($\gamma \geq 7.4$, LAGB $\geq$ 70 %), most of these LAGBs were retained, and only a few of them evolved into HAGBs with further straining. Importantly, LAGBs even survived in CoCrFeNi-based HEAs during very high temperature annealing [75,76]. The lifetime of a LAGB from generation to annihilation in HEAs appears to be significantly longer than that in conventional materials [28–30,77], and thus it seems that LAGBs in CoCrFeNi alloys are very stable.

As depicted in the region (B) in Fig. 7, the propagation of Shockley partial dislocation is accompanied by trailing a single-layer nanotwin and ending a SF. It is known that nanotwinned structures with low excess energy are quite stable at very high stresses [61]. Likewise, SFs also possess low excess energy and further contribute to even higher stability in CoCrFeNi alloys [42,78,79]. The high densities of low-energy configurations (LAGBs, nanotwins, and SFs) observed here can explain the high stability of the microstructure after HPT processing.

During twin-dominated hardening in stage (C), numerous Shockley partial dislocations were emitted from GBs, the fraction of which was saturated at a grain size of about 54 nm, Fig. 5(b). This dislocation emission process may induce GB relaxation and decrease the GB energy [80], further enhancing the stability of GBs. In the nanocrystalline copper, low-energy configurations are analogous to the present study, namely nanotwins and SFs, which exhibit high thermal stability below a critical grain size of 70 nm [81]. Thus a high thermal stability of the nanocrystalline CoCrFeNi alloys can be suggested. It is worth noting that the high density of LAGBs during straining indicates that recrystallization processes did not prevail, revealing a high stability of the grain size in CoCrFeNi alloys under deformation conditions.

The above reasons for the exceptional microstructural stability of nanocrystalline CoCrFeNi alloys are discussed from the perspective of the phase structure, the low-energy configurations (LAGBs, nanotwins, and SFs), and the grain size. This implies that CoCrFeNi alloys or CoCrFeNi-based HEAs exhibit a potential for developing stable nanostructured alloys for high-temperature applications. However, He et al. [14] have found evidence of phase separation in CoCrFeNi after long-term annealing (1023 K for 800 h). As such, further investigation is required to optimize the structures of CoCrFeNi-based HEAs for high-temperature applications.

4.4. Capacity for strain energy storage

In the present part, the excess energy in the nanograin after 10 HPT rotations is estimated by the strains from the GPA estimation. A low elastic anisotropy factor of 1.91 in the CoCrFeNi alloy was reported [82], and isotropic elasticity is thus assumed. Therefore, the strain energy, $E_\mathrm{strain}^\mathrm{isotropic}$, can be roughly estimated by the following expression [83]:

$$E_\mathrm{strain}^\mathrm{isotropic} = \left(\frac{9}{2} \bullet \mu\left(\frac{E-2\mu}{3\mu-E}\right) + 3\mu\right) \bullet V_0\varepsilon^2 \tag{3}$$

where μ is the shear modulus (84 GPa [68]), E is the Young's modulus (227 GPa), which was determined by nanoindentation measurements. V_0 denotes the molar volume (6.874×10^{-6} m^3 mol^{-1}), and ε is the average of the principal strains, i.e. ε_{xx}, ε_{yy}, and ε_{zz}. For molar volume calculation, the density (8.2 g cm^{-3}) was measured at room temperature using the buoyancy method based on Archimedes' principle. An average principal strain (ε) of about 1.1 % in the grain interior was estimated by the GPA method, details can be found in Appendix D. Finally, a strain energy of 952 J mol^{-1} or 17 J g^{-1} is obtained.

DSC measurements as shown in Fig. 8 were conducted using various heating rates on the HPT-processed samples with 10 rotations and a mass of about 50 mg. Significant exothermic peaks between 600 and 890 K were observed, likely due to heat release during recrystallization. Consequently, an average strain energy of around 18.49 J g^{-1} was calculated. This finding closely aligns with the stored energy estimated using the GPA method [83].

While the temporal deformation mechanisms and the microstructural features were investigated in the present CoCrFeNi alloy, there are still some important issues that remain unresolved.

1. Regarding the deformation mechanisms, how does the detwinning mechanism work in CoCrFeNi alloys?
2. Activation of the twinning process in nanograins according to the classic twinning mechanism involves overcoming a high barrier.

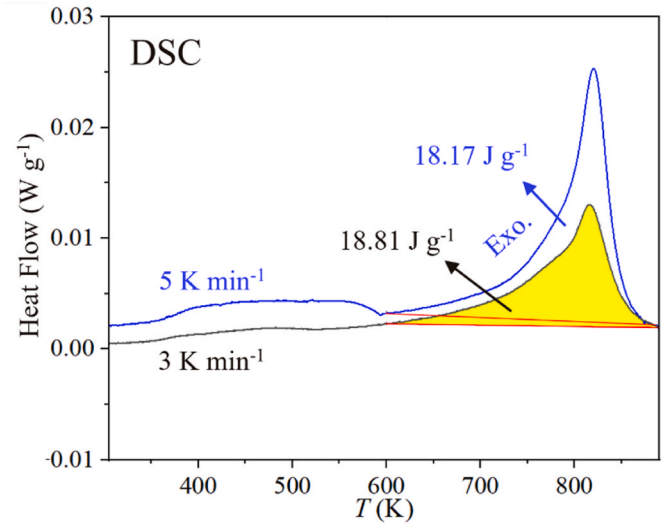

Fig. 8. DSC heat flow curves at different heating rates after 10 HPT rotations and the corresponding exothermic peaks showing the strain energy release after recrystallization.

However, numerous twins were actually formed inside the grains, Fig. 6. Creating defects in nanocrystalline materials appears to occur readily in CoCrFeNi alloys, and the reasons for the high capacity for defect storage within nanograins, where distances to the nearest sinks are always short, still need to be investigated further.

3. A high stability of the deformation-induced microstructures was clarified, especially concerning the LAGBs. The capacity of LAGB resistance for recrystallization is very high in CoCrFeNi HEAs, however, there are still some LAGBs evolving into HAGBs during straining. To develop stable nanostructured alloys for high-temperature applications, a stable and high resistance against recrystallization or a more effective method to impede the annihilation of LAGBs in CoCrFeNi alloys could present improved approaches.

5. Conclusions

Hardness and microstructural evolution of the HPT-processed CoCrFeNi alloys were systemically studied by XRD, EBSD, and TEM. The deformation mechanisms, their dependence on the total (accumulated) strain, the associated microstructural characteristics, and the strain energy of the nanocrystalline CoCrFeNi alloys were discussed. The following conclusions are drawn.

1. A three-stage hardening mechanism for the deformed CoCrFeNi alloys was indicated: (i) Initially, a rapid increase in hardness was attributed to the sharp increase in the density of LAGBs, accompanied by a high density of dislocations. (ii) With continued straining, a fraction of the LAGBs evolved into HAGBs, completing grain boundary strengthening. (iii) A remarkable increase in hardness was achieved in the final stage of hardness enhancement, primarily due to the formation of numerous twins within nanograins, which were mainly formed by the emission of Shockley partial dislocations from GBs.
2. Shockley partial dislocations were identified, and a critical stress of about 2.16 GPa for twin nucleation in the nanoscale grains was estimated. Low-energy configurations (LAGBs, nanotwins, and SFs) favor the high stability of the deformation-induced microstructures, and further contribute to the high thermal stability of the nanocrystalline or ultrafine grained material after HPT processing. The high fraction of LAGBs reveals a high stability of the grain size, and thus CoCrFeNi alloys or CoCrFeNi-based HEAs exhibit a potential for developing stable nanostructured alloys for high-temperature applications. An estimate of the average strain within nanograins after 10 HPT rotations yielded a value of about 1.1 % and the corresponding strain energy was identified to about 17 J g^{-1}.

CRediT authorship contribution statement

Haihong Jiang: Writing – original draft, Visualization, Methodology, Investigation, Data curation, Conceptualization. **Qingmei Gong:** Writing – review & editing, Investigation, Data curation. **Martin Peterlechner:** Writing – review & editing, Supervision, Data curation. **Lydia Daum:** Writing – review & editing, Data curation. **Harald Rösner:** Writing – review & editing, Supervision, Methodology. **Gerhard Wilde:** Writing – review & editing, Supervision, Methodology, Conceptualization.

Declaration of competing interest

The authors declare that they have no known competing financial interests or personal relationships that could have appeared to influence the work reported in this paper.

Data availability

No data was used for the research described in the article.

Acknowledgments

Haihong Jiang and Qingmei Gong sincerely acknowledge funding by the China Scholarship Council program. Financial support by the German Research Foundation (DFG) under the grant (WI1899/32–2; SPP 2006) is gratefully acknowledged. Christoph Gammer (ESI Leoben) is acknowledged for providing his template matching code for strain analysis via nanobeam diffraction patterns

Appendix A. Supplementary data

Supplementary data to this article can be found online at https://doi.org/10.1016/j.msea.2024.146758.

References

[1] W. Li, D. Xie, D. Li, Y. Zhang, Y. Gao, P.K. Liaw, Mechanical behavior of high-entropy alloys, Prog. Mater. Sci. 118 (2021) 100777, https://doi.org/10.1016/j.pmatsci.2021.100777.
[2] D.B. Miracle, O.N. Senkov, A critical review of high entropy alloys and related concepts, Acta Mater. 122 (2017) 448–511, https://doi.org/10.1016/j.actamat.2016.08.081.
[3] J. Gubicza, P.T. Hung, M. Kawasaki, J.-K. Han, Y. Zhao, Y. Xue, J.L. Lábár, Influence of severe plastic deformation on the microstructure and hardness of a CoCrFeNi high-entropy alloy: a comparison with CoCrFeNiMn, Mater. Char. 154 (2019) 304–314, https://doi.org/10.1016/j.matchar.2019.06.015.
[4] P.T. Hung, M. Kawasaki, J.-K. Han, J.L. Lábár, J. Gubicza, Microstructure evolution in a nanocrystalline CoCrFeNi multi-principal element alloy during annealing, Mater. Char. 171 (2021) 110807, https://doi.org/10.1016/j.matchar.2020.110807.
[5] P. Sathiyamoorthi, J. Basu, S. Kashyap, K. Pradeep, R.S. Kottada, Thermal stability and grain boundary strengthening in ultrafine-grained CoCrFeNi high entropy alloy composite, Mater. Des. 134 (2017) 426–433, https://doi.org/10.1016/j.matdes.2017.08.053.
[6] S.N. Naik, S.M. Walley, The Hall-Petch and inverse Hall-Petch relations and the hardness of nanocrystalline metals, J. Mater. Sci. 55 (2020) 2661–2681, https://doi.org/10.1007/s10853-019-04160-w.
[7] M.A. Meyers, A. Mishra, D.J. Benson, Mechanical properties of nanocrystalline materials, Prog. Mater. Sci. 51 (2006) 427–556, https://doi.org/10.1016/j.pmatsci.2005.08.003.
[8] R. Valiev, Nanostructuring of metals by severe plastic deformation for advanced properties, Nat. Mater. 3 (2004) 511–516, https://doi.org/10.1038/nmat1180.
[9] B. Wang, H. He, M. Naeem, S. Lan, S. Harjo, T. Kawasaki, Y. Nie, H. Kui, T. Ungar, D. Ma, A.D. Stoica, Q. Li, Y. Ke, C.T. Liu, X.L. Wang, Deformation of CoCrFeNi high entropy alloy at large strain, Scripta Mater. 155 (2018) 54–57, https://doi.org/10.1016/j.scriptamat.2018.06.013.

[10] H. Jiang, Q. Gong, M. Peterlechner, S.V. Divinski, G. Wilde, Microstructure analysis of a CoCrFeNi high-entropy alloy after compressive deformation, Mater. Sci. Eng. 888 (2023) 145785, https://doi.org/10.1016/j.msea.2023.145785.
[11] W. Zhao, J.-K. Han, Y.O. Kuzminova, S.A. Evlashin, A.P. Zhilyaev, A.M. Pesin, J.-i. Jang, K.D. Liss, M. Kawasaki, Significance of grain refinement on micro-mechanical properties and structures of additively-manufactured CoCrFeNi high-entropy alloy, Mater. Sci. Eng. 807 (2021) 140898, https://doi.org/10.1016/j.msea.2021.140898.
[12] P.T. Hung, M. Kawasaki, J.-K. Han, Á. Szabó, J.L. Lábár, Z. Hegedűs, J. Gubicza, Thermal stability of nanocrystalline CoCrFeNi multi-principal element alloy: effect of the degree of severe plastic deformation, Intermetallics 142 (2022) 107445, https://doi.org/10.1016/j.intermet.2021.107445.
[13] Z. Zhang, Z. Jiang, Y. Xie, S.L.I. Chan, J. Liang, J. Wang, Multiple deformation mechanisms induced by pre-twinning in CoCrFeNi high entropy alloy, Scripta Mater. 207 (2022) 114266, https://doi.org/10.1016/j.scriptamat.2021.114266.
[14] F. He, Z. Wang, Q. Wu, J. Li, J. Wang, C. Liu, Phase separation of metastable CoCrFeNi high entropy alloy at intermediate temperatures, Scripta Mater. 126 (2017) 15–19, https://doi.org/10.1016/j.scriptamat.2016.08.008.
[15] G. Williamson, R. Smallman III, Dislocation densities in some annealed and cold-worked metals from measurements on the X-ray debye-scherrer spectrum, Philos. Mag. A 1 (1956) 34–46, https://doi.org/10.1080/14786435608238074.
[16] R. Smallman, K. Westmacott, Stacking faults in face-centred cubic metals and alloys, Philos. Mag. A 2 (1957) 669–683, https://doi.org/10.1080/14786435708242709.
[17] A. Saastamoinen, A. Kaijalainen, D. Porter, P. Suikkanen, J.-R. Yang, Y.-T. Tsai, The effect of finish rolling temperature and tempering on the microstructure, mechanical properties and dislocation density of direct-quenched steel, Mater. Char. 139 (2018) 1–10, https://doi.org/10.1016/j.matchar.2018.02.026.
[18] C. Gammer, J. Kacher, C. Czarnik, O. Warren, J. Ciston, A. Minor, Local and transient nanoscale strain mapping during in situ deformation, Appl. Phys. Lett. 109 (2016) 081906, https://doi.org/10.1063/1.4961683.
[19] V. Ozdol, C. Gammer, X. Jin, P. Ercius, C. Ophus, J. Ciston, A. Minor, Strain mapping at nanometer resolution using advanced nano-beam electron diffraction, Appl. Phys. Lett. 106 (2015) 253107, https://doi.org/10.1063/1.4922994.
[20] M.J. Hÿtch, E. Snoeck, R. Kilaas, Quantitative measurement of displacement and strain fields from HRTEM micrographs, Ultramicroscopy 74 (1998) 131–146, https://doi.org/10.1016/S0304-3991(98)00035-7.
[21] A.V. Podolskiy, Y.O. Shapovalov, E.D. Tabachnikova, A.S. Tortika, M. A. Tikhonovsky, B. Joni, E. Odor, T. Ungar, S. Maier, C. Rentenberger, M. J. Zehetbauer, E. Schafler, Anomalous evolution of strength and microstructure of high-entropy alloy CoCrFeNiMn after high-pressure torsion at 300 and 77 K, Adv. Eng. Mater. 22 (2020) 1900752, https://doi.org/10.1002/adem.201900752.
[22] B. Schuh, F. Mendez-Martin, B. Völker, E.P. George, H. Clemens, R. Pippan, A. Hohenwarter, Mechanical properties, microstructure and thermal stability of a nanocrystalline CoCrFeMnNi high-entropy alloy after severe plastic deformation, Acta Mater. 96 (2015) 258–268, https://doi.org/10.1016/j.actamat.2015.06.025.
[23] P. Nagy, N. Rohbeck, G. Roussely, P. Sortais, J.L. Lábár, J. Gubicza, J. Michler, L. Pethö, Processing and characterization of a multibeam sputtered nanocrystalline CoCrFeNi high-entropy alloy film, Surf. Coating. Technol. 386 (2020) 125465, https://doi.org/10.1016/j.surfcoat.2020.125465.
[24] B. Clausen, T. Lorentzen, T. Leffers, Self-consistent modelling of the plastic deformation of fcc polycrystals and its implications for diffraction measurements of internal stresses, Acta Mater. 46 (1998) 3087–3098, https://doi.org/10.1016/S1359-6454(98)00014-7.
[25] S. Yoshida, T. Ikeuchi, T. Bhattacharjee, Y. Bai, A. Shibata, N. Tsuji, Effect of elemental combination on friction stress and Hall-Petch relationship in face-centered cubic high/medium entropy alloys, Acta Mater. 171 (2019) 201–215, https://doi.org/10.1016/j.actamat.2019.04.017.
[26] Y. Zhong, D. Ping, X. Song, F. Yin, Determination of grain size by XRD profile analysis and TEM counting in nano-structured Cu, J. Alloys Compd. 476 (2009) 113–117, https://doi.org/10.1016/j.jallcom.2008.08.075.
[27] F. Dalla Torre, R. Lapovok, J. Sandlin, P.F. Thomson, C.H.J. Davies, E.V. Pereloma, Microstructures and properties of copper processed by equal channel angular extrusion for 1-16 passes, Acta Mater. 52 (2004) 4819–4832, https://doi.org/10.1016/j.actamat.2004.06.040.
[28] A. Belyakov, T. Sakai, H. Miura, K. Tsuzaki, Grain refinement in copper under large strain deformation, Philos. Mag. A 81 (2001) 2629–2643, https://doi.org/10.1080/01418610108216659.
[29] Y. Ito, Z. Horita, Microstructural evolution in pure aluminum processed by high-pressure torsion, Mater. Sci. Eng. 503 (2009) 32–36, https://doi.org/10.1016/j.msea.2008.03.055.
[30] A. Belyakov, Y. Kimura, K. Tsuzaki, Microstructure evolution in dual-phase stainless steel during severe deformation, Acta Mater. 54 (2006) 2521–2532, https://doi.org/10.1016/j.actamat.2006.01.035.
[31] W. Xu, X. Liu, K. Lu, Strain-induced microstructure refinement in pure Al below 100 nm in size, Acta Mater. 152 (2018) 138–147, https://doi.org/10.1016/j.actamat.2018.04.014.
[32] W.T. Read, W. Shockley, Dislocation models of crystal grain boundaries, Phys. Rev. 78 (1950) 275–289, https://doi.org/10.1103/PhysRev.78.275.
[33] M.J. Hÿtch, J.-L. Putaux, J. Thibault, Stress and strain around grain-boundary dislocations measured by high-resolution electron microscopy, Philos. Mag. A 86 (2006) 4641–4656, https://doi.org/10.1080/14786430600743876.
[34] T. Csanádi, M. Bl'anda, N.Q. Chinh, P. Hvizdoš, J. Dusza, Orientation-dependent hardness and nanoindentation-induced deformation mechanisms of WC crystals, Acta Mater. 83 (2015) 397–407, https://doi.org/10.1016/j.actamat.2014.09.048.
[35] X. An, S. Ni, M. Song, X. Liao, Deformation twinning and detwinning in face-centered cubic metallic materials, Adv. Eng. Mater. 22 (2020) 1900479, https://doi.org/10.1002/adem.201900479.
[36] X. Liao, Y. Zhao, S. Srinivasan, Y. Zhu, R. Valiev, D. Gunderov, Deformation twinning in nanocrystalline copper at room temperature and low strain rate, Appl. Phys. Lett. 84 (2004) 592–594, https://doi.org/10.1063/1.1644051.
[37] X. Wu, X. Liao, S. Srinivasan, F. Zhou, E. Lavernia, R. Valiev, Y. Zhu, New deformation twinning mechanism generates zero macroscopic strain in nanocrystalline metals, Phys. Rev. Lett. 100 (2008) 095701, https://doi.org/10.1103/PhysRevLett.100.095701.
[38] X. Ma, H. Zhou, J. Narayan, Y. Zhu, Stacking-fault energy effect on zero-strain deformation twinning in nanocrystalline Cu-Zn alloys, Scripta Mater. 109 (2015) 89–93, https://doi.org/10.1016/j.scriptamat.2015.07.027.
[39] Y. Zhu, X. Liao, X. Wu, Deformation twinning in nanocrystalline materials, Prog. Mater. Sci. 57 (2012) 1–62, https://doi.org/10.1016/j.pmatsci.2011.05.001.
[40] T. Zhu, J. Li, A. Samanta, H.G. Kim, S. Suresh, Interfacial plasticity governs strain rate sensitivity and ductility in nanostructured metals, Proc. Natl. Acad. Sci. USA 104 (2007) 3031–3036, https://doi.org/10.1073/pnas.0611097104.
[41] K. Lu, L. Lu, S. Suresh, Strengthening materials by engineering coherent internal boundaries at the nanoscale, science 324 (2009) 349–352, https://doi.org/10.1126/science.1159610.
[42] J. Xiao, N. Wu, O. Ojo, C. Deng, Stacking fault and transformation-induced plasticity in nanocrystalline high-entropy alloys, J. Mater. Res. 36 (2021) 2705–2714, https://doi.org/10.1557/s43578-021-00140-6.
[43] Q. Pan, L. Zhang, R. Feng, Q. Lu, K. An, A.C. Chuang, J.D. Poplawsky, P.K. Liaw, L. Lu, Gradient cell-structured high-entropy alloy with exceptional strength and ductility, Science 374 (2021) 984–989, https://doi.org/10.1126/science.abj8114.
[44] S. Praveen, J.W. Bae, P. Asghari-Rad, J.M. Park, H.S. Kim, Ultra-high tensile strength nanocrystalline CoCrNi equi-atomic medium entropy alloy processed by high-pressure torsion, Mater. Sci. Eng. 735 (2018) 394–397, https://doi.org/10.1016/j.msea.2018.08.079.
[45] L. Lu, Y. Shen, X. Chen, L. Qian, K. Lu, Ultrahigh strength and high electrical conductivity in copper, Science 304 (2004) 422–426, https://doi.org/10.1126/science.1092905.
[46] Y. Zhao, T. Yang, Y. Tong, J. Wang, J. Luan, Z. Jiao, D. Chen, Y. Yang, A. Hu, C. Liu, J. Kai, Heterogeneous precipitation behavior and stacking-fault-mediated deformation in a CoCrNi-based medium-entropy alloy, Acta Mater. 138 (2017) 72–82, https://doi.org/10.1016/j.actamat.2017.07.029.
[47] M. Kumar, A.J. Schwartz, W.E. King, Microstructural evolution during grain boundary engineering of low to medium stacking fault energy fcc materials, Acta Mater. 50 (2002) 2599–2612, https://doi.org/10.1016/S1359-6454(02)00090-3.
[48] H. Rösner, C. Kübel, Y. Ivanisenko, L. Kurmanaeva, S.V. Divinski, M. Peterlechner, G. Wilde, Strain mapping of a triple junction in nanocrystalline Pd, Acta Mater. 59 (2011) 7380–7387, https://doi.org/10.1016/j.actamat.2011.08.020.
[49] D.-H. Lee, I.-C. Choi, M.-Y. Seok, J. He, Z. Lu, J.-Y. Suh, M. Kawasaki, T. G. Langdon, J.-i. Jang, Nanomechanical behavior and structural stability of a nanocrystalline CoCrFeNiMn high-entropy alloy processed by high-pressure torsion, J. Mater. Res. 30 (2015) 2804–2815, https://doi.org/10.1557/jmr.2015.239.
[50] P. Yu, H. Cheng, L. Zhang, H. Zhang, Q. Jing, M. Ma, P. Liaw, G. Li, R. Liu, Effects of high pressure torsion on microstructures and properties of an Al0.1CoCrFeNi high-entropy alloy, Mater. Sci. Eng. 655 (2016) 283–291, https://doi.org/10.1016/j.msea.2015.12.085.
[51] J. Jung, J.I. Yoon, J.G. Kim, M.I. Latypov, J.Y. Kim, H.S. Kim, Continuum understanding of twin formation near grain boundaries of FCC metals with low stacking fault energy, npj Comput. Mater. 3 (2017) 21, https://doi.org/10.1038/s41524-017-0023-1.
[52] A. Shabani, M.R. Toroghinejad, M. Aminaei, P. Cavaliere, Dynamic recrystallization nanoarchitectonics of FeCrCuMnNi multi-phase high entropy alloy, J. Alloys Compd. 968 (2023) 172001, https://doi.org/10.1016/j.jallcom.2023.172001.
[53] S. Wu, G. Wang, J. Yi, Y. Jia, I. Hussain, Q. Zhai, P. Liaw, Strong grain-size effect on deformation twinning of an Al0.1CoCrFeNi high-entropy alloy, Mater. Res. Lett. 5 (2017) 276–283, https://doi.org/10.1080/21663831.2016.1257514.
[54] K. Rahman, V. Vorontsov, D. Dye, The effect of grain size on the twin initiation stress in a TWIP steel, Acta Mater. 89 (2015) 247–257, https://doi.org/10.1016/j.actamat.2015.02.008.
[55] C. Pande, K. Cooper, Nanomechanics of Hall-Petch relationship in nanocrystalline materials, Prog. Mater. Sci. 54 (2009) 689–706, https://doi.org/10.1016/j.pmatsci.2009.03.008.
[56] Z.C. Cordero, B.E. Knight, C.A. Schuh, Are nanotwinned structures in fcc metals optimal for strength, ductility and grain stability studies on pure metals, Int. Mater. Rev. 61 (2016) 495–512, https://doi.org/10.1080/09506608.2016.1191808.
[57] S. Gourdet, F. Montheillet, A model of continuous dynamic recrystallization, Acta Mater. 51 (2003) 2685–2699, https://doi.org/10.1016/S1359-6454(03)00078-8.
[58] G. Dyakonov, S. Mironov, I. Semenova, R. Valiev, S. Semiatin, Microstructure evolution and strengthening mechanisms in commercial-purity titanium subjected to equal-channel angular pressing, Mater. Sci. Eng. 701 (2017) 289–301, https://doi.org/10.1016/j.msea.2017.06.079.
[59] J. Hu, Y. Shi, X. Sauvage, G. Sha, K. Lu, Grain boundary stability governs hardening and softening in extremely fine nanograined metals, Science 355 (2017) 1292–1296, https://doi.org/10.1126/science.aal5166.
[60] Y.T. Zhu, T.G. Langdon, Influence of grain size on deformation mechanisms: an extension to nanocrystalline materials, Mater. Sci. Eng. 409 (2005) 234–242, https://doi.org/10.1016/j.msea.2005.05.111.

[61] Y. Kulkarni, R.J. Asaro, D. Farkas, Are nanotwinned structures in fcc metals optimal for strength, ductility and grain stability? Scripta Mater. 60 (2009) 532–535, https://doi.org/10.1016/j.scriptamat.2008.12.007.
[62] Y. Zhang, J. Wang, H. Shan, K. Zhao, Strengthening high-stacking-fault-energy metals via parallelogram nanotwins, Scripta Mater. 108 (2015) 35–39, https://doi.org/10.1016/j.scriptamat.2015.05.039.
[63] W. Huo, F. Fang, X. Liu, S. Tan, Z. Xie, J. Jiang, Remarkable strain-rate sensitivity of nanotwinned CoCrFeNi alloys, Appl. Phys. Lett. 114 (2019) 101904, https://doi.org/10.1063/1.5088921.
[64] J. Venables, On dislocation pole models for twinning, Philos. Mag. A 30 (1974) 1165–1169, https://doi.org/10.1080/14786437408207269.
[65] P. Pirouz, Deformation mode in silicon, slip or twinning? Scripta Metall. 21 (1987) 1463–1468, https://doi.org/10.1016/0036-9748(87)90284-5.
[66] J. Cohen, J. Weertman, A dislocation model for twinning in fcc metals, Acta Metall. 11 (1963) 996–998, https://doi.org/10.1016/0001-6160(63)90074-9.
[67] K. Lagerlöf, J. Castaing, P. Pirouz, A. Heuer, Nucleation and growth of deformation twins: a perspective based on the double-cross-slip mechanism of deformation twinning, Philos. Mag. A 82 (2002) 2841–2854, https://doi.org/10.1080/01418610208240069.
[68] Z. Wu, H. Bei, G.M. Pharr, E.P. George, Temperature dependence of the mechanical properties of equiatomic solid solution alloys with face-centered cubic crystal structures, Acta Mater. 81 (428) (2014) 428–441, https://doi.org/10.1016/j.actamat.2014.08.026.
[69] Y. Zhao, Z. Horita, T. Langdon, Y. Zhu, Evolution of defect structures during cold rolling of ultrafine-grained Cu and Cu-Zn alloys: influence of stacking fault energy, Mater. Sci. Eng. 474 (2008) 342–347, https://doi.org/10.1016/j.msea.2007.06.014.
[70] Z. Luo, X. Guo, J. Hou, X. Zhou, X. Li, K. Lu, Plastic deformation induced hexagonal-close packed nickel nano-grains, Scripta Mater. 168 (2019) 67–70, https://doi.org/10.1016/j.scriptamat.2019.04.024.
[71] M.S. Dodaran, S. Guo, M.M. Khonsari, N. Shamsaei, S. Shao, A theoretical calculation of stacking fault energy of Ni alloys: the effects of temperature and composition, Comput. Mater. Sci. 191 (2021) 110326, https://doi.org/10.1016/j.commatsci.2021.110326.
[72] H. Shahmir, P. Asghari-Rad, M.S. Mehranpour, F. Forghani, H.S. Kim, M. Nili-Ahmadabadi, Evidence of FCC to HCP and BCC-martensitic transformations in a CoCrFeNiMn high-entropy alloy by severe plastic deformation, Mater. Sci. Eng. 807 (2021) 140875, https://doi.org/10.1016/j.msea.2021.140875.
[73] S. Huang, W. Li, S. Lu, F. Tian, J. Shen, E. Holmström, L. Vitos, Temperature dependent stacking fault energy of FeCrCoNiMn high entropy alloy, Scripta Mater. 108 (2015) 44–47, https://doi.org/10.1016/j.scriptamat.2015.05.041.
[74] Y. Wang, B. Liu, K. Yan, M. Wang, S. Kabra, Y.-L. Chiu, D. Dye, P.D. Lee, Y. Liu, B. Cai, Probing deformation mechanisms of a FeCoCrNi high-entropy alloy at 293 and 77 K using in situ neutron diffraction, Acta Mater. 154 (2018) 79–89, https://doi.org/10.1016/j.actamat.2018.05.013.
[75] N. Fan, A. Rafferty, R. Lupoi, W. Li, Y. Xie, S. Yin, Microstructure evolution and mechanical behavior of additively manufactured CoCrFeNi high-entropy alloy fabricated via cold spraying and post-annealing, Mater. Sci. Eng. 873 (2023) 144748, https://doi.org/10.1016/j.msea.2023.144748.
[76] L.A. Santos, S. Singh, A.D. Rollett, Microstructure and texture evolution during thermomechanical processing of Al0.25CoCrFeNi high-entropy alloy, Metall. Mater. Trans. A 50 (2019) 5433–5444, https://doi.org/10.1007/s11661-019-05399-3.
[77] H. Li, T. Chen, W. Li, H. Zhang, S. Han, C. Zhou, Z. Chen, E.A. Flores-Johnson, L. Shen, J. Lian, I.J. Beyerlein, X. Liao, Grain size dependent microstructure and texture evolution during dynamic deformation of nanocrystalline face-centered cubic materials, Acta Mater. 216 (2021) 117088, https://doi.org/10.1016/j.actamat.2021.117088.
[78] F. He, Z. Wang, Q. Wu, D. Chen, T. Yang, J. Li, J. Wang, C. Liu, J.-j. Kai, Tuning the defects in face centered cubic high entropy alloy via temperature-dependent stacking fault energy, Scripta Mater. 155 (2018) 134–138, https://doi.org/10.1016/j.scriptamat.2018.06.002.
[79] Q. Pan, M. Yang, R. Feng, A.C. Chuang, K. An, P.K. Liaw, X. Wu, N. Tao, L. Lu, Atomic faulting induced exceptional cryogenic strain hardening in gradient cell-structured alloy, Science 382 (2023) 185–190, https://doi.org/10.1126/science.adj3974.
[80] J. Rittner, D.N. Seidman, K. Merkle, Grain-boundary dissociation by the emission of stacking faults, Phys. Rev. B 53 (1996) R4241, https://doi.org/10.1103/PhysRevB.53.R4241.
[81] X. Zhou, X. Li, K. Lu, Enhanced thermal stability of nanograined metals below a critical grain size, Science 360 (2018) 526–530, https://doi.org/10.1126/science.aar6941.
[82] N.E. Koval, J.I. Juaristi, R.D. Muiño, M. Alducin, Structure and properties of CoCrFeNiX multi-principal element alloys from ab initio calculations, J. Appl. Phys. 127 (2020) 145102, https://doi.org/10.1063/1.5142239.
[83] H. Rösner, N. Boucharat, K. Padmanabhan, J. Markmann, G. Wilde, Strain mapping in a deformation-twinned nanocrystalline Pd grain, Acta Mater. 58 (2010) 2610–2620, https://doi.org/10.1016/j.actamat.2009.12.047.